European Journal of Radiology 117 (2019) 49–55

Contents lists available at ScienceDirect

European Journal of Radiology

journal homepage: www.elsevier.com/locate/ejrad

Virtual monoenergetic images from spectral detector CT as a surrogate for conventional CT images: Unaltered attenuation characteristics with reduced image noise

Nils Große Hokamp[a,b,c,*], R. Gilkeson[b,c], M.K. Jordan[b], K.R. Laukamp[b,c], Victor-Frederick Neuhaus[a], S. Haneder[a], S.S. Halliburton[d], A. Gupta[b,c]

[a] IUniversity of Cologne, Faculty of Medicine and University Hospital Cologne, Institute for Diagnostic and Interventional Radiology, Cologne, Germany
[b] Department of Radiology, Case Western Reserve University, Cleveland, OH, USA
[c] Department of Radiology, University Hospitals Medical Center, Cleveland, OH, USA
[d] Philips Healthcare, Clinical Science CT, Cleveland OH, USA

ARTICLE INFO

Keywords:
Dual energy computed tomography
Virtual monoenergetic images
Image reconstruction
Spectral detector computed tomography

ABSTRACT

Objective: This study aimed to identify the energy level of virtual monoenergetic images (VMI) that closest represents conventional images (CI) in order to demonstrate that these images provide improved image quality in terms of noise and Signal-to-noise ratio (SD/SNR) while attenuation values (HU) remain unaltered as compared to CI.

Methods: 60 and 30 patients with contrast-enhanced (CE) and non-enhanced (NCE) spectral detector CT (SDCT) of the abdomen were included in this retrospective, IRB-approved study. CI and VMI of 66–74 keV as well as quantitative iodine maps were reconstructed (Q-IodMap). Two regions of interest were placed in each: pulmonary trunk, abdominal aorta, portal vein, liver, pancreas, renal cortex left/right, psoas muscle, (filled) bladder and subcutaneous fat. For each reconstruction, HU and SD were averaged. ΔHU and SNR (SNR = HU/SD) were calculated. Q-IodMap were considered as confounder for ΔHU. In addition, two radiologists compared VMI of 72 keV and CI in a forced-choice approach regarding image quality.

Results: In NCE studies, no significant differences for any region was found. In CE studies, VMI_{72keV} images showed lowest ΔHU (HU_{liver} CI/VMI_{72keV}: 104 ± 18/103 ± 17, $p \geq 0.05$). Iodine containing voxels as indicated by Q-IodMap resulted in an over- and underestimation of attenuation in lower and higher VMI energies, respectively. Image noise was lower in VMI images (e.g. muscle: CI/ VMI_{72keV}: 15.3 ± 3.3/12.3 ± 2.9 HU, $p \leq 0.05$). Hence, SNR was significantly higher in VMI_{72keV} compared to CI (e.g. liver 3.8 ± 0.6 vs 3.0 ± 0.8, $p \leq 0.05$). In visual analysis, VMI_{72keV} were preferred over CI at all times.

Conclusions: VMI_{72keV} show improved SD/SNR characteristics while the attenuation remains unaltered as compared to CI.

1. Introduction

Although proposed in the early days of computed tomography (CT), dual energy CT (DECT) did not become clinically available until the late 2000s [1,2]. While conventional CT measures integrated attenuation of all energies of a polychromatic X-ray spectrum, attenuation for low and high energies are separated in DECT [2]. Different approaches to DECT are clinically available and classified as either emission- or detection-based [3]. Approaches for emission-based concepts are dual-source computed tomography (DSCT), kV_p-switching DECT and twin-beam DECT, while spectral detector computed tomography (SDCT) is the only detector-based approach to DECT [3]. SDCT is equipped with a dual layer detector that preferentially detects low energy photons in its top layer and high energy photons in its bottom layer [4].

DECT allows for computation of virtual monoenergetic images (VMI) approximating images that would result from acquisition at a

Abbreviations: CT, computed tomography; DECT, dual energy computed tomography; DSCT, dual source computed tomography; SDCT, spectral detector computed tomography; VMI, virtual monoenergetic images; (N)CE, (non) contrast-enhanced; $CTDI_{vol}$, volumetric computed tomography dose index; CI, conventional image; SNR, signal-to-noise ratio

* Corresponding author at: Institute for Diagnostic and Interventional Radiology, University Hospital Cologne, Cologne, Kerpener Str. 62, 50937 Köln, Germany.
E-mail address: nils.grosse-hokamp@uk-koeln.de (N. Große Hokamp).

https://doi.org/10.1016/j.ejrad.2019.05.019
Received 20 February 2019; Received in revised form 23 April 2019; Accepted 25 May 2019

single X-ray energy level expressed in units of kiloelectron volts (keV). Depending on the DECT-approach, they are available in a range of 40–200 keV and obtained from linear blending of low and high energy attenuation profiles [5]. Attenuation values (measured in Hounsfield units) change with the keV level [5–7]. As compared to conventional images, attenuation is greater in low keV images and decreases with increasing keV (except for fat, which shows inverse characteristics). By definition water and air will always have 0 HU and -1024 HU, respectively, in a perfectly calibrated (DE)CT system. VMIs derived from x-ray projection data (rather than image data) are associated with lower noise compared to conventional images at all keV levels [7–9]. Projection based image reconstruction is possible in SDCT-imaging due to temporal and spatial coherence of low and high energy projection data [10,11]. In addition, VMI at higher keV have been shown to be less susceptible to beam hardening artifacts compared to conventional images., [12–15].

The average photon energy for a polychromatic X-ray spectrum depends on the peak tube voltage applied. The average energy also varies across scanner models, particularly models from different manufacturers, because of design differences such as x-ray filtration. For SDCT, the average energy for a peak tube voltage of 120 kVp has been reported to be between 68–75 keV [7]. Therefore, it is expected that VMIs with an energy level within this range will would yield attenuation values that most closely match conventional images; however, to the authors' best knowledge, no study has systematically investigated this in patients. As evaluation of CT density is part of the diagnostic interpretation of a CT scan, a close agreement with conventional images is highly desirable if using VMI in the clinical routine.

This study aims to compare virtual monoenergetic images of different energies to conventional images in order to 1) demonstrate that VMI comprise a mean of noise reduction and to 2) identify a keV level that combines the low noise characteristics of VMI with unaltered attenuation as compared to conventional images.

2. Materials and methods

2.1. Patient population

All patients ≥ 18 years that underwent SDCT examination between 01/08/2017 and 01/02/2018 on a clinical SDCT scanner (IQon, Philips Healthcare, Cleveland, USA) were included in this institutional review board approved, Health Insurance Portability and Accountability Act-compliant retrospective study. There was a waiver for informed written consent under Code of Federal Regulations (title 45, §46.116d). In this analysis we included 60 consecutive patients who underwent contrast enhanced SDCT of chest, abdomen and pelvis and 30 patients with unenhanced examinations of the same body regions (CE and NCE studies, respectively). All examinations were carried out with the imaging protocol described below. Patients with image artifacts due to motion or implants and with incomplete image reconstructions were excluded from further assessment.

2.2. Image acquisition and reconstruction

All studies were acquired in a head first, supine position. For contrast enhanced studies, intravenous access was established through an antecubital vein. Contrast media (Optiray 350, Guerbet, Bloomington, IN, USA) volume was bodyweight-adapted and injected at a flow rate of 3 ml/s. Image acquisition was started with a delay of 80 s after contrast injection. Tube voltage for both CE and NCE examinations was set to 120 kVp and tube current modulation was enabled in all patients (DoseRight 3D-DOM, Philips Healthcare, Cleveland, USA). The field of view was adapted to the patient size and, due to the detector-based approach, dual energy information was obtained over the entire field of view. Additional scan parameters were identical for CE and NCE examinations: rotation time = 0.33 s, pitch = 0.98, collimation = 64 x 0.625 mm and matrix = 512 × 512. The volumetric computed tomography dose index ($CTDI_{vol}$) was recorded for each examination.

Conventional images (CI) were reconstructed using a hybrid iterative reconstruction algorithm (iDose^4, Philips Healthcare, Cleveland, USA), while VMI were reconstructed using a dedicated spectral reconstruction algorithm (Spectral, Kernel B, denoising level 3, Philips Healthcare, Cleveland, USA). All images were reconstructed with a slice thickness of 3 mm. VMI were reconstructed at energy levels of 66 keV, 68 keV, 70 keV, 72 keV and 74 keV. Energy levels were chosen according to earlier reports and the vendor-claimed keV-equivalent of 70 keV [7]. Due to the boost of iodine-associated attenuation and its role as possible confounder in differences between CI and VMI, iodine concentration maps were also computed. All reconstructions were carried out using clinically available software and algorithms from the vendor.

2.3. Image analysis

Two regions of interest were drawn in each of the following structures: Pulmonary trunk, abdominal aorta, portal vein, liver, pancreas, renal cortex left/right, psoas muscle, (filled) bladder and subcutaneous fat, resulting in a total of 18 ROIs. ROIs were kept at a constant area of 100 mm^2, placed in CI and transferred to identical positions in VMI and Iodine density maps using the vendor's proprietary image viewer (IntelliSpace Portal, Philips Healthcare, Best, The Netherlands). Attenuation and standard deviation (HU and SD [HU], for CI and VMI) as well as the iodine concentration ([mg/ml]) were recorded and averaged for repetitive measurements. Standard deviation within the fat was considered indicative of image noise. The difference in attenuation between CI and the different VMI levels was calculated as $\Delta HU = HU_{VMI} - HU_{CI}$. Additionally, the signal-to-noise ratio for a ROI was calculated as $SNR_x = {HU_x}/{SD_x}$.

2.4. Subjective analysis

Two radiologists with 3 and 4 years experience in CT imaging independently reviewed CI and VMI_{72keV} images side-by-side blinded to the reconstruction technique. Based on a forced-choice comparison, they determined the superior reconstruction. Readers were instructed to consider image sharpness, noise and contrast in their decision.

2.5. Statistics

All analyses were carried out using JMP Software (SAS Institute, Cary, USA). Data are presented as mean ± standard deviation. ANOVA with appropriate post hoc testing for multiple adjustments was used (Tukey and Dunnett for comparisons versus CI and between all CI and VMI, respectively). The correlation between Δ HU and iodine concentration was assessed by means of Pearson correlation and further visualized using waterfall plots. P-values ≤ 0.05 were considered statistically significant.

3. Results

A total of 90 patients were included in the final analysis. Of these 48 were men, while 42 were women. Mean age was 63.0 ± 13.9 years. $CTDI_{vol}$ was 11.5 ± 6.4 mGy.

3.1. Attenuation

Detailed attenuation values for NCE studies are reported in Table 1. In NCE studies, attenuation between CI and VMI did not differ significantly except for fat (p ≤ 0.05). Here, VMI_{74keV} showed significantly higher attenuation than CI (-105.3 ± 11.5 HU versus -96.4 ± 11.2 HU, p ≤ 0.05).

Table 1
Attenuation values.

	ROI	CI	66keV	68keV	70keV	72keV	74 keV
NCE	**Aorta**	33.5 ± 16.6	36.6 ± 8.0	36.6 ± 7.7	34.2 ± 15.3	36.5 ± 7.1	36.6 ± 6.9
	Pulmonary trunk	37.7 ± 7.0	38.3 ± 7.5	38.1 ± 7.2	38.1 ± 6.9	38.0 ± 6.7	37.9 ± 6.5
	Portal vein	35.4 ± 7.2	34.5 ± 7.6	34.7 ± 7.2	34.3 ± 7.0	34.8 ± 6.6	34.9 ± 6.4
	Liver	48.9 ± 19.7	51.5 ± 8.0	51.9 ± 7.8	48.8 ± 19.5	52.4 ± 7.4	52.7 ± 7.3
	Pancreas	39.7 ± 7.3	38.1 ± 8.1	38.2 ± 7.8	38.3 ± 7.8	38.2 ± 7.4	38.2 ± 7.2
	Kidney	33.9 ± 9.3	32.9 ± 10.7	32.9 ± 10.0	33.2 ± 9.4	33.0 ± 9.0	33.0 ± 8.5
	Bladder	7.8 ± 12.1	7.9 ± 12.7	8.2 ± 12.6	8.5 ± 12.6	8.8 ± 12.6	9.1 ± 12.6
	Muscle	44.5 ± 8.5	42.8 ± 9.3	42.9 ± 9.0	43.0 ± 8.8	43.1 ± 8.6	43.2 ± 8.4
	Fat	−104.5 ± 12.0	−105.5 ± 12.3	−102.9 ± 11.9	−100.7 ± 11.7	−98.3 ± 11.5	−96.4 ± 11.2
CE	**Aorta**	212.0 ± 42.8	254.3 ± 54.0	240.0 ± 50.4	226.9 ± 47.1	215.1 ± 44.0	204.4 ± 41.2
	Pulmonary trunk	203.0 ± 44.6	235.6 ± 56.8	222.3 ± 53.0	210.1 ± 49.7	199.2 ± 46.5	189.1 ± 43.7
	Portal vein	173.0 ± 32.2	205.8 ± 40.6	194.7 ± 37.9	184.5 ± 35.2	175.4 ± 33.1	167.1 ± 31.0
	Liver	104.0 ± 17.9	112.8 ± 20.7	109.1 ± 19.5	105.9 ± 18.5	102.7 ± 17.5	99.9 ± 16.7
	Pancreas	102.0 ± 19.6	114.5 ± 22.6	109.4 ± 21.3	105.0 ± 20.3	100.5 ± 19.2	96.6 ± 18.3
	Kidney	186.9 ± 33.4	215.7 ± 37.0	203.8 ± 34.6	190.8 ± 34.2	183.0 ± 30.4	174.0 ± 28.6
	Bladder	8.3 ± 10.7	11.0 ± 11.3	11.0 ± 10.8	11.0 ± 10.5	11.0 ± 10.1	11.0 ± 9.8
	Muscle	56.7 ± 10.5	57.9 ± 6.3	57.3 ± 6.1	57.9 ± 10.7	56.2 ± 5.7	55.8 ± 5.6
	Fat	−107.7 ± 8.1	−108.2 ± 8.2	−105.7 ± 7.9	−103.6 ± 7.7	−101.5 ± 7.5	−99.6 ± 7.3

Average attenution values for various regions of interest in unenhanced and contrast enhanced examination (NCE and CE). Values are reported for conventional images (CI) and virtual monoenergetic images of various energies (66–68 keV).

In CE studies, overall attenuation between CI and VMI differed more compared to NCE studies (Table 1). VMI_{66keV} displayed higher attenuation of all vessels and organs ($p \leq 0.05$). Higher attenuation was also found in VMI_{68keV} for organs with high iodine content, e.g. the aorta and the renal cortex ($p \leq 0.05$). Tissue with very little or no resting perfusion (i.e. the psoas muscle and bladder) did not exhibit any significant difference between CI and VMI of any level ($p \geq 0.05$).

The overall Δ HU in NCE studies did not differ significantly between VMI (Table 2). Yet, a tendency towards lower attenuation in low keV images was again observed (VMI_{66keV}: -0.5 ± 2.8 HU, VMI_{68keV}: -0.1 ± 2.7 HU, VMI_{70keV}: -0.2 ± 2.7 HU, VMI_{72keV}: 0.5 ± 3.3 HU and VMI_{74keV}: 0.8 ± 3.7 HU; $p \geq 0.05$). In CE studies the opposite was found, with higher attenuation in low keV images (VMI_{66keV}: 17.3 ± 17.1 HU, VMI_{68keV}: 11.1 ± 11.1 HU, VMI_{70keV}: 5.4 ± 6.5 HU, VMI_{72keV}: 0.3 ± 5.3 HU and VMI_{74keV}: 4.4 ± 8.0 HU; $p \leq 0.05$).

Correlation between Δ HU and iodine concentration ranged from 0.01 – 0.80 (Fig. 2; $p \leq 0.05$). For VMI_{72keV} we found a random correlation (R^2 of 0.01). Accordingly, a shift from overestimation of iodine-containing ROI towards their underestimation can be depicted from the waterfall plots (Figs. 1 and 2); however, in VMI_{72keV} a rather random distribution of over- and underestimation in dependency of iodine concentration is found.

3.2. Noise

Image noise was significantly lower in VMI as compared to CI for both CE and NCE studies (e.g. CI / VMI_{72keV} 14.6 ± 2.0 / 12.1 ± 1.6 HU for NCE and 13.4 ± 2.1 / 11.0 ± 1.8 HU for CE; $p \leq 0.05$, Fig. 3). Between the various keV levels image noise did not differ ($p \geq 0.05$).

3.3. Signal-to-noise ratio

As per definition the reduced noise in combination with just slightly altered attenuation in VMI_{72keV} resulted in a significant improvement of SNR as compared to CI (Table 3). In NCE studies, SNR improvement failed to reach significance for the portal vein, the renal cortex, the bladder and the muscle. In CE studies all SNR were significantly improved in VMI_{72keV} except for the bladder.

3.4. Visual image assessment

Both radiologists preferred the VMI_{72keV} over the CI image in every

Table 2
ΔHU for different energy levels.

	ROI	66keV	68keV	70keV	72keV	74 keV
NCE	**Aorta**	−2.9 ± 13.8	−3.0 ± 13.9	−0.7 ± 3.9	−2.9 ± 14.0	−3.0 ± 14.2
	Pulmonary trunk	−0.6 ± 1.2	−0.5 ± 0.9	−0.4 ± 0.8	−0.3 ± 0.9	−0.2 ± 1.2
	Portal vein	0.9 ± 3.3	0.7 ± 3.1	1.0 ± 1.7	0.6 ± 3.1	0.5 ± 3.1
	Liver	−2.6 ± 18.2	−2.9 ± 18.0	0.1 ± 0.9	−3.4 ± 17.9	−3.7 ± 17.8
	Pancreas	1.6 ± 1.9	1.5 ± 1.6	1.4 ± 1.4	1.5 ± 1.4	1.5 ± 1.3
	Kidney	0.7 ± 3.1	0.7 ± 2.6	0.7 ± 2.2	0.7 ± 2.1	0.7 ± 2.1
	Bladder	−0.1 ± 5.0	−0.4 ± 5.1	−0.7 ± 5.3	−1.0 ± 5.5	−1.3 ± 5.7
	Muscle	1.7 ± 2.6	1.5 ± 2.3	1.4 ± 2.2	1.3 ± 2.2	1.2 ± 2.1
	Fat	1.0 ± 1.8	−1.6 ± 1.7	−3.7 ± 1.8	−5.9 ± 2.0	−7.8 ± 2.3
CE	**Aorta**	−40.9 ± 14.4	−27.1 ± 10.4	−14.5 ± 7.1	−3.1 ± 5.0	7.4 ± 5.2
	Pulmonary trunk	−32.1 ± 14.4	−19.0 ± 10.8	−6.9 ± 8.0	3.8 ± 6.2	13.7 ± 6.0
	Portal vein	−31.8 ± 11.0	−21.1 ± 7.9	−11.2 ± 5.4	−2.4 ± 3.9	5.7 ± 3.9
	Liver	−8.5 ± 3.7	−4.9 ± 2.6	−1.8 ± 1.8	1.3 ± 1.6	4.0 ± 2.1
	Pancreas	−12.1 ± 4.9	−7.2 ± 3.6	−2.9 ± 2.7	1.5 ± 2.4	5.2 ± 2.7
	Kidney	−27.9 ± 18.2	−16.4 ± 16.8	−3.8 ± 5.6	3.7 ± 15.7	12.5 ± 15.8
	Bladder	−2.6 ± 4.7	−2.6 ± 4.6	−2.6 ± 4.6	−2.6 ± 4.6	−2.6 ± 4.7
	Muscle	−1.1 ± 8.9	−0.5 ± 8.8	−1.2 ± 2.7	0.5 ± 8.8	0.9 ± 8.8
	Fat	0.5 ± 1.7	−1.9 ± 1.6	−3.9 ± 1.6	−6.0 ± 1.8	−7.9 ± 2.0

Average difference between virtual monoenergetic images and conventional images (ΔHU) for various regions of interest in unenhanced and contrast enhanced examinations (NCE and CE). Values are reported for virtual monoenergetic images of various energies (66–68 keV).

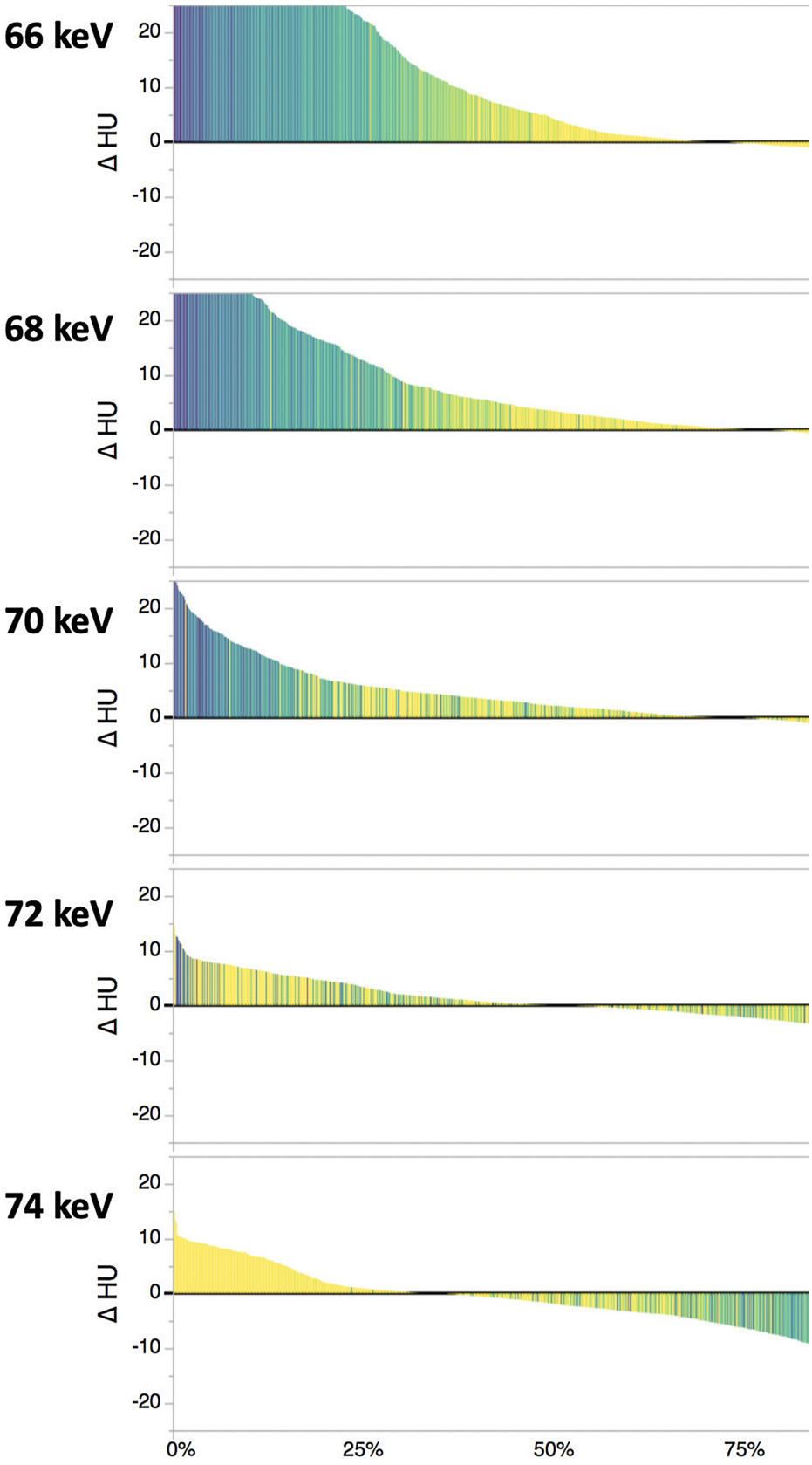

Fig. 1. Waterfall plots highlighting differences between conventional images and virtual monoenergetic images of various energies in CE studies (Δ HU in A). In addition, the average iodine concentration is indicated using a color scale; this clearly visualizes a shift from overestimation of iodine-associated attenuation in 66–70 keV images towards a random effect of iodine in 72 keV images towards its underestimation in 74 keV images.

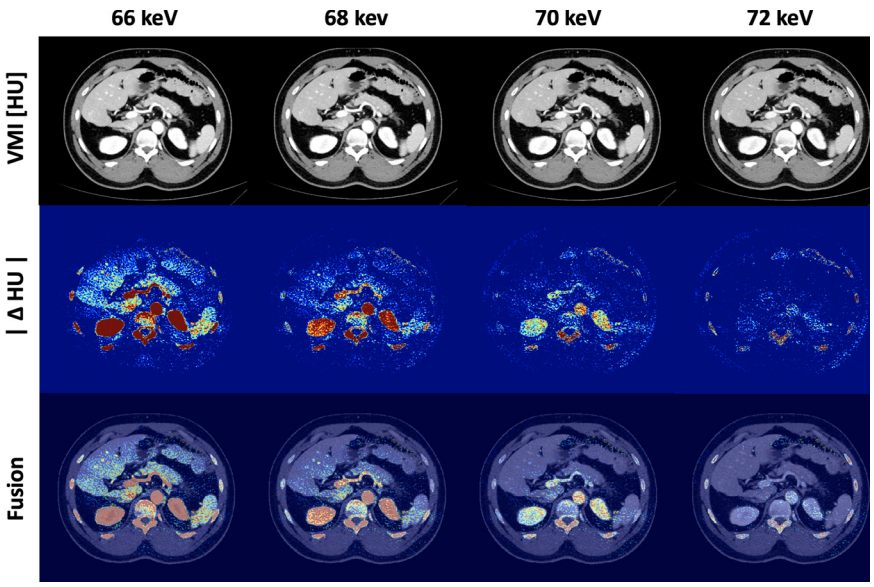

Fig. 2. Example images of a 51-year old patient as virtual monoenergetic images of 66–74 keV (upper row). Further Δ HU [CI; VMI]. Δ HU is visualized in a color-coded image (center row) and in a fused image of CI and Δ HU (lower row). Note, that offset is visually greatest in high-attenuation pixels (i.e. vasculature, renal cortex and (cortical) bone.

case (100%).

4. Discussion

This study aimed to demonstrate, that VMI comprise a mean of noise reduction and to identify the equivalent energy level of VMI for representation of conventional images while benefiting from their lower noise characteristics. We report that there indeed are differences among energy levels between 66 keV – 74 keV in CE studies, while differences in NCE examinations are negligible. Minimal offset for CE studies was found in VMI_{72keV} images which yield superior SNR as compared to CI. Further, visual analysis clearly demonstrated a favor towards VMI_{72keV} over CI.

Noise reduction has been a main focus since the introduction of CT imaging [14,16,17]. Image noise is typically dominated by quantum noise or the statistical uncertainty in the number of x-ray photons collected to form an image which is determined by a number of acquisition, detection and reconstruction related scanner features and/or parameters as well as patient factors such as size. Some scanner related factors such as tube output or image reconstruction algorithm (e.g., iterative reconstruction versus filtered back projection) can be influenced by the user while others like detector efficiency are fixed for a given system.

VMI are less susceptible to beam hardening and therefore noise; nevertheless, this benefit may be outweighed by noise induced during the material decomposition process for some dual energy CT solutions [18–20]. Due to the detector-based approach of SDCT, the low and high energy attenuation information is temporally and spatially registered enabling material decomposition within the x-ray projection domain [9,11]. By linear combination of information from lower and upper detector layer, VMIs can be computed. Projection space decomposition allows the identification and removal of anti-correlated noise resulting in noise suppression as indicated by our results and earlier studies [6,10,13,15]. VMI from other DECT require angular interpolation for image reconstruction within the projection domain (kVp switching DECT) or only allow for image reconstruction within the image space domain (dual source DECT, twin beam DECT). Although kVp switching DECT enables projection domain processing after angular interpolation, studies demonstrated that this comes with a penalty in image noise as compared to conventional images obtained at the same radiation dose [21–25]. For dual source DECT and twin-beam DECT, computation of dual energy results is enabled in the image domain only, therefore VMI from these systems carry a noise-penalty as compared to CI when using comparable radiation doses [23,26–28] although improvements in VMI creation from dual source DECT data have partly addressed this inherent limitation [27–31]. Characteristics, noise and SNR differ between the different systems; however, the few available studies on this focus on low energy VMI reporting that noise is significantly lower in SDCT as compared to DSCT systems [5,32]. In particular, no study is available that evaluates VMI of a level comparable to CI, despite such cross vendor comparison is greatly desirable.

In VMI from SDCT, noise reduction results from physics-driven data

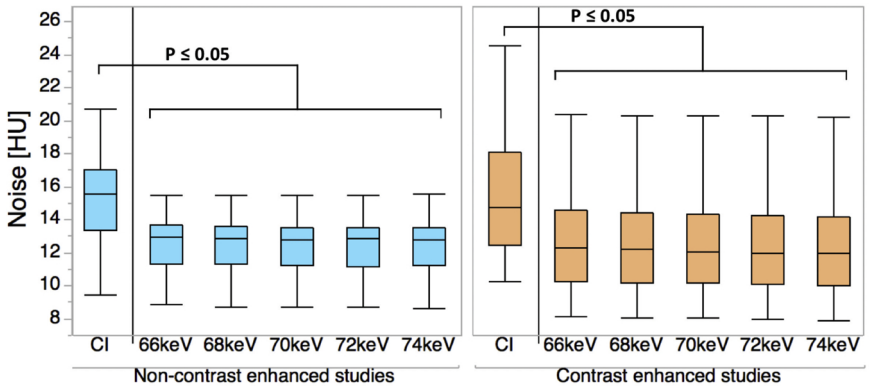

Fig. 3. Noise as indicated by standard deviation of region of interest measurements within the psoas muscle in unenhanced and contrast enhanced examination. Values are reported for conventional images (CI) and virtual monoenergetic images of 66–74 keV. Significant differences as compared to CI are indicated.

Table 3
SNR values.

	NCE			CE		
ROI	CI	VMI_{72keV}	p-value	CI	VMI_{72keV}	p-value
Aorta	2.0 ± 0.7	2.5 ± 0.7	0.0125*	11.3 ± 2.8	13.8 ± 3.2	< .0001*
PT	4.0 ± 1.0	4.8 ± 1.2	0.0046*	16.5 ± 3.5	19.9 ± 4.5	< .0001*
VP	2.0 ± 0.6	2.4 ± 0.7	0.0565	8.9 ± 2.1	10.8 ± 2.6	< .0001*
Liver	3.0 ± 0.8	3.8 ± 0.6	0.0001*	5.2 ± 1.2	5.9 ± 1.4	0.0053*
Panc	2.2 ± 0.5	2.6 ± 0.6	0.0139*	5.2 ± 1.4	6.1 ± 1.7	0.0017*
Kidney	2.3 ± 0.8	2.7 ± 1.0	0.0822	11.3 ± 3.1	12.8 ± 3.5	0.0113*
Bladder	0.6 ± 0.5	0.8 ± 0.7	0.2269	0.6 ± 0.6	0.9 ± 0.7	0.0687
Muscle	2.5 ± 0.7	2.9 ± 0.9	0.0589	3.0 ± 0.8	3.7 ± 0.9	< .0001*
Fat	7.3 ± 1.2	8.3 ± 1.5	0.0079*	8.2 ± 1.6	9.5 ± 1.8	< .0001*

Signal-to-noise ratios for various regions of interest in unenhanced and contrast enhanced examination (NCE and CE). Values are reported for conventional images (CI) and virtual monoenergetic images of 72 keV. P-values for comparison between both groups are reported, significant differences are indicated by an asterisk.

processing (i.e. exploitation of anti-correlation of noise) which differs from means of iterative image reconstruction [19,22,29]. VMI are obtained by linear blending of information from both detector layers. While further details on the exact process of image reconstruction are proprietary to the vendor; it is reasonable to assume that some sort of nonlinear noise reduction is integrated in the image computation of VMI. It remains elusive if this is due the fact that reconstruction of SDCT images that contain anticorrelated noise in the individual detector data sets is a nonlinear process itself or due to additional iterative image processing [7]. To account for this, the conventional images that served as baseline were reconstructed using a hybrid-iterative image reconstruction algorithm instead of filtered-back projection; further, the denoising level remained unaltered on a medium setting between CI and VMI.

CT allows for quantitative measurements of attenuation and these measurements are frequently considered in clinical decision making, e.g. a cysts are expected to exhibit attenuation between -20 and +20 HU and an adrenal lesion is consistent with an adenoma if its attenuation on NCE is < 10 HU [33,34]. Although attenuation, particularly of contrast enhanced tissue, is much higher in lower keV images (e.g. 40 keV) and much lower in higher keV images (e.g. 200 keV), attenuation values at a keV level similar to the average energy of a polychromatic beam generated for conventional imaging are equivalent. VMIs with significantly different attenuation values may require some training regarding their interpretation for clinical decision making; however, when attenuation values are similar to conventional images this training may be omitted.

While the average energy of a polychromatic X-ray spectrum is frequently reported to be 70–75 keV and multiple vendors therefore consider VMI_{70keV} images to provide attenuation values equivalent to CI; we demonstrated that this results in an overestimation of attenuation, especially in contrast enhanced studies. Instead, we identified VMI_{72keV} to show closest agreement with CI with a significant increase of SNR and to suggest superiority over CI; however, the energy level will likely differ in other DECT-approaches or possibly even in different protocol settings. Regarding radiation dose, our study is comparable to other studies [35,36].

We conducted a confounder analysis for iodine concentration which indicated a random influence of iodine density on attenuation in VMI_{72keV}. Hence, we consider our results independent of contrast injection parameters; however, some differences may occur in different image acquisition protocols. Besides iodine, high attenuation caused by bone resulted in a greater visual difference between CI and VMI; however, we deliberately refrained from a quantitative analysis of bone attenuation differences due to the impossibility of reproducible and accurate ROI placement.

There are some additional limitations that need to be addressed. First, our results are limited to examinations using 120 kVp and comparable imaging protocols. Further, the appropriate keV level could change if a significant shift in average x-ray energy for a given kVp occurs over time with aging of the X-ray tube (or detector). Second, iterative reconstruction is frequently attributed to the risk of loss in image detail while the approach of VMI_{72keV} is associated with a reduction of anti-correlated noise, therefore loss of image information seems to be less likely; however, further studies are needed to investigate this further (especially in terms of spatial resolution). Last, we only included a limited number of patients; however, this small cohort yielded clear and significant results. Future, large-scale studies should consider a variety of different protocols.

Virtual monoenergetic images at an energy of 72 keV show the same attenuation characteristics as conventional 120 kVp images for both contrast-enhanced and non-contrast examinations while exhibiting significantly lower image noise. This results in a significant improvement in SNR. Our data suggests using 72 keV for noise reduction by means of VMI without altering image attenuation.

Disclosures

NGH is on the speaker's bureau of Philips Healthcare. SSH is an employee of Philips Healthcare and was not involved in data acquisition, handling, statistical analysis or interpretion. All other authors declare no conflict of interest.

Funding

Parts of this study were funded under a research agreement between University Hospitals Cleveland Medical Center, Case Western Reserve University and Philips Healthcare.

References

[1] T.G. Flohr, C.H. McCollough, H. Bruder, M. Petersilka, K. Gruber, C. Süss, M. Grasruck, K. Stierstorfer, B. Krauss, R. Raupach, A.N. Primak, A. Küttner, S. Achenbach, C. Becker, A. Kopp, B.M. Ohnesorge, First performance evaluation of a dual-source CT (DSCT) system, Eur. Radiol. 16 (2006) 256–268, https://doi.org/10.1007/s00330-005-2919-2.
[2] R.E. Alvarez, A. Macovski, Energy-selective reconstructions in X-ray computerized tomography, Phys. Med. Biol. 21 (1976) 733–744, https://doi.org/10.1088/0031-9155/21/5/002.
[3] C.H. McCollough, S. Leng, L. Yu, J.G. Fletcher, Dual- and multi-energy CT: principles, technical approaches, and clinical applications, Radiology 276 (2015) 637–653, https://doi.org/10.1148/radiol.2015142631.
[4] E. Shefer, A. Altman, R. Behling, R. Goshen, L. Gregorian, Y. Roterman, I. Uman, N. Wainer, Y. Yagil, O. Zarchin, State of the art of CT detectors and sources: a literature review, Curr. Radiol. Rep. 1 (2013) 76–91, https://doi.org/10.1007/s40134-012-0006-4.
[5] M.C. Jacobsen, D. Schellingerhout, C.A. Wood, E.P. Tamm, M.C. Godoy, J. Sun, D.D. Cody, Intermanufacturer comparison of dual-energy CT iodine quantification and monochromatic attenuation: a phantom study, Radiology 287 (2018) 224–234, https://doi.org/10.1148/radiol.2017170896.
[6] V. Neuhaus, N. Große Hokamp, N. Abdullayev, R. Rau, A. Mpotsaris, D. Maintz, J. Borggrefe, Metal artifact reduction by dual-layer computed tomography using virtual monoenergetic images, Eur. J. Radiol. 93 (2017) 143–148, https://doi.org/

10.1016/j.ejrad.2017.05.013.
[7] O. Ozguner, A. Dhanantwari, S. Halliburton, G. Wen, S. Utrup, D. Jordan, Objective image characterization of a spectral CT scanner with dual-layer detector, Phys. Med. Biol. 63 (2018) 025–027, https://doi.org/10.1088/1361-6560/aa9e1b.
[8] N. Große Hokamp, R. Kessner, S. Van Hedent, F.P. Graner, A. Gupta, R. Gilkeson, Spectral detector computed tomography pulmonary angiography: improved diagnostic assessment and automated estimation of window settings, J. Comput. Assist. Tomogr. 42 (2018) 850–857, https://doi.org/10.1097/RCT.0000000000000743.
[9] K.M. Brown, S. Zabic, G. Shechter, Impact of spectral separation in dual-energy CT with anti-correlated statistical reconstruction, Proc. 13th Fully Three-Dimensional Image Reconstr. Radiol. Nucl. Med, (2015), pp. 491–494.
[10] N. Große Hokamp, A.J. Höink, J. Doerner, D.W. Jordan, G. Pahn, T. Persigehl, D. Maintz, S. Haneder, Assessment of arterially hyper-enhancing liver lesions using virtual monoenergetic images from spectral detector CT: phantom and patient experience, Abdom. Radiol. (New York) 43 (2018) 2066–2074, https://doi.org/10.1007/s00261-017-1411-1.
[11] N. Große Hokamp, J. Salem, A. Hesse, J.A. Holz, M. Ritter, A. Heidenreich, D. Maintz, S. Haneder, Low-dose characterization of kidney stones using spectral detector computed tomography: an ex vivo study, Invest. Radiol. 53 (2018) 457–462, https://doi.org/10.1097/RLI.0000000000000468.
[12] N. Große Hokamp, K.R. Laukamp, S. Lennartz, D. Zopfs, N. Abdullayev, V.F. Neuhaus, D. Maintz, J. Borggrefe, Artifact reduction from dental implants using virtual monoenergetic reconstructions from novel spectral detector CT, Eur. J. Radiol. 104 (2018) 136–142, https://doi.org/10.1016/j.ejrad.2018.04.018.
[13] K. Kalisz, N. Rassouli, A. Dhanantwari, D. Jordan, P. Rajiah, Noise characteristics of virtual monoenergetic images from a novel detector-based spectral CT scanner, Eur. J. Radiol. 98 (2018) 118–125, https://doi.org/10.1016/j.ejrad.2017.11.005.
[14] F. Kelcz, P.M. Joseph, S.K. Hilal, Noise considerations in dual energy CT scanning, Med. Phys. 6 (1979) 418–425, https://doi.org/10.1118/1.594520.
[15] N. Große Hokamp, A. Hellerbach, A. Gierich, D.W. Jordan, V. Visser-Vandewalle, D. Maintz, S. Haneder, Reduction of artifacts caused by deep brain stimulating electrodes in cranial computed tomography imaging by means of virtual monoenergetic images, metal artifact reduction algorithms, and their combination, Invest. Radiol. 53 (2018) 424–431, https://doi.org/10.1097/RLI.0000000000000460.
[16] B. Heismann, M. Balda, Quantitative image-based spectral reconstruction for computed tomography, Med. Phys. 36 (2009) 4471–4485, https://doi.org/10.1118/1.3213534.
[17] R.C. Nelson, S. Feuerlein, D.T. Boll, New iterative reconstruction techniques for cardiovascular computed tomography: How do they work, and what are the advantages and disadvantages? J. Cardiovasc. Comput. Tomogr. 5 (2011) 286–292, https://doi.org/10.1016/j.jcct.2011.07.001.
[18] S. Leng, L. Yu, J. Wang, J.G. Fletcher, C.A. Mistretta, C.H. McCollough, Noise reduction in spectral CT: reducing dose and breaking the trade-off between image noise and energy bin selection, Med. Phys. 38 (2011) 4946–4957, https://doi.org/10.1118/1.3609097.
[19] C. Maass, M. Baer, M. Kachelriess, Image-based dual energy CT using optimized precorrection functions: a practical new approach of material decomposition in image domain, Med. Phys. 36 (2009) 3818–3829, https://doi.org/10.1118/1.3157235.
[20] R. Fahmi, B.L. Eck, J. Levi, A. Fares, A. Dhanantwari, M. Vembar, H.G. Bezerra, D.L. Wilson, Quantitative myocardial perfusion imaging in a porcine ischemia model using a prototype spectral detector CT system, Phys. Med. Biol. 61 (2016) 2407–2431, https://doi.org/10.1088/0031-9155/61/6/2407.
[21] K. Matsumoto, M. Jinzaki, Y. Tanami, A. Ueno, M. Yamada, S. Kuribayashi, Virtual monochromatic spectral imaging with fast kilovoltage switching: improved image quality as compared with that obtained with conventional 120-kVp CT, Radiology 259 (2011) 257–262, https://doi.org/10.1148/radiol.11100978.
[22] R. Alvarez, E. Seppi, A comparison of noise and dose in conventional and energy selective computed tomography, IEEE Trans. Nucl. Sci. 26 (1979) 2853–2856, https://doi.org/10.1109/TNS.1979.4330549.
[23] L. Yu, S. Leng, C.H. McCollough, Dual-energy CT-based monochromatic imaging, AJR Am. J. Roentgenol. 199 (2012) 9–15, https://doi.org/10.2214/AJR.12.9121.
[24] D. Zhang, X. Li, B. Liu, Objective characterization of GE discovery CT750 HD scanner: gemstone spectral imaging mode, Med. Phys. 38 (2011) 1178–1188, https://doi.org/10.1118/1.3551999.
[25] B. Li, G. Yadava, J. Hsieh, Quantification of head and body CTDI(VOL) of dual-energy x-ray CT with fast-kVp switching, Med. Phys. 38 (2011) 2595–2601, https://doi.org/10.1118/1.3582701.
[26] A. Euler, M.M. Obmann, Z. Szucs-Farkas, A. Mileto, C. Zaehringer, A.L. Falkowski, D.J. Winkel, D. Marin, B. Stieltjes, B. Krauss, S.T. Schindera, Comparison of image quality and radiation dose between split-filter dual-energy images and single-energy images in single-source abdominal CT, Eur. Radiol. 28 (2018) 3405–3412, https://doi.org/10.1007/s00330-018-5338-x.
[27] D.B. Husarik, S. Gordic, L. Desbiolles, B. Krauss, S. Leschka, S. Wildermuth, H. Alkadhi, Advanced virtual monoenergetic computed tomography of hyperattenuating and hypoattenuating liver lesions, Invest. Radiol. 50 (2015) 695–702, https://doi.org/10.1097/RLI.0000000000000171.
[28] T. D'Angelo, A.M. Bucher, L. Lenga, C.T. Arendt, J.L. Peterke, D. Caruso, S. Mazziotti, A. Blandino, G. Ascenti, A.E. Othman, S.S. Martin, D. Leithner, T.J. Vogl, J.L. Wichmann, Optimisation of window settings for traditional and noise-optimised virtual monoenergetic imaging in dual-energy computed tomography pulmonary angiography, Eur. Radiol. 28 (2018) 1393–1401, https://doi.org/10.1007/s00330-017-5059-6.
[29] S. Ehn, T. Sellerer, D. Muenzel, A.A. Fingerle, F. Kopp, M. Duda, K. Mei, B. Renger, J. Herzen, J. Dangelmaier, B.J. Schwaiger, A. Sauter, I. Riederer, M. Renz, R. Braren, E.J. Rummeny, F. Pfeiffer, P.B. Noel, Assessment of quantification accuracy and image quality of a full-body dual-layer spectral CT system, J. Appl. Clin. Med. Phys. (2017), https://doi.org/10.1002/acm2.12243.
[30] C.N. De Cecco, D. Caruso, U.J. Schoepf, D. De Santis, G. Muscogiuri, M.H. Albrecht, F.G. Meinel, J.L. Wichmann, P.F. Burchett, A. Varga-Szemes, D.H. Sheafor, A.D. Hardie, A noise-optimized virtual monoenergetic reconstruction algorithm improves the diagnostic accuracy of late hepatic arterial phase dual-energy CT for the detection of hypervascular liver lesions, Eur. Radiol. 28 (2018) 3393–3404, https://doi.org/10.1007/s00330-018-5313-6.
[31] D. Caruso, A.H. Parinella, U.J. Schoepf, M.H. Stroebel, S. Mangold, J.L. Wichmann, A. Varga-Szemes, B.D. Ball, D. De Santis, A. Laghi, C.N. De Cecco, Optimization of window settings for standard and advanced virtual monoenergetic imaging in abdominal dual-energy CT angiography, Abdom. Radiol. 42 (2017) 772–780, https://doi.org/10.1007/s00261-016-0963-9.
[32] T. Sellerer, P.B. Noël, M. Patino, A. Parakh, S. Ehn, S. Zeiter, J.A. Holz, J. Hammel, A.A. Fingerle, F. Pfeiffer, D. Maintz, E.J. Rummeny, D. Muenzel, D.V. Sahani, Dual-energy CT: a phantom comparison of different platforms for abdominal imaging, Eur. Radiol. (2018), https://doi.org/10.1007/s00330-017-5238-5.
[33] M.A. Bosniak, The current radiological approach to renal cysts, Radiology 158 (1986) 1–10, https://doi.org/10.1148/radiology.158.1.3510019.
[34] N. Schieda, E.S. Siegelman, Update on CT and MRI of adrenal nodules, Am. J. Roentgenol. 208 (2017) 1206–1217, https://doi.org/10.2214/AJR.16.17758.
[35] U. Mahmood, N. Horvat, J.V. Horvat, D. Ryan, Y. Gao, G. Carollo, R. DeOcampo, R.K. Do, S. Katz, S. Gerst, C.R. Schmidtlein, L. Dauer, Y. Erdi, L. Mannelli, Rapid switching kVp dual energy CT: value of reconstructed dual energy CT images and organ dose assessment in multiphasic liver CT exams, Eur. J. Radiol. 102 (2018) 102–108, https://doi.org/10.1016/j.ejrad.2018.02.022.
[36] N. Große Hokamp, V.C. Obmann, R. Kessner, K.R. Laukamp, T. Persigehl, S. Haneder, N. Ramaiya, Improved visualization of hypodense liver lesions in virtual monoenergetic images from spectral detector CT: proof of concept in a 3D-printed phantom and evaluation in 74 patients, Eur. J. Radiol. 109 (2018) 114–123, https://doi.org/10.1016/j.ejrad.2018.11.001.